

# Electrothermal domains in stacks of intrinsic Josephson junctions in $\text{Bi}_2\text{Sr}_2\text{CaCu}_2\text{O}_8$

B. Gross,<sup>1</sup> S. Guénon,<sup>1,2</sup> J. Yuan,<sup>3</sup> M.Y. Li,<sup>3,4</sup> J. Li,<sup>3</sup> A. Iishi,<sup>3</sup> R.G. Mints,<sup>5</sup>

T. Hatano,<sup>3</sup> P.H. Wu,<sup>4</sup> D. Koelle,<sup>1</sup> H.B. Wang,<sup>3,4,\*</sup> and R. Kleiner<sup>1,†</sup>

<sup>1</sup>*Physikalisches Institut – Experimentalphysik II and Center for Collective Quantum Phenomena in LISA<sup>+</sup>, Universität Tübingen, Auf der Morgenstelle 14, D-72076 Tübingen, Germany*

<sup>2</sup>*Department of Physics, Center for Advanced Nanoscience, University of California-San Diego, La Jolla, California 92093, USA*

<sup>3</sup>*National Institute for Materials Science, Tsukuba 3050047, Japan*

<sup>4</sup>*Research Institute of Superconductor Electronics, Nanjing University, Nanjing 210093, China*

<sup>5</sup>*The Raymond and Beverly Sackler School of Physics and Astronomy, Tel Aviv University, Tel Aviv 69978, Israel*

(Dated: December 26, 2021)

We have studied experimentally and numerically temperature profiles and the formation of electrothermal domains (“hot spots”) in  $\text{Bi}_2\text{Sr}_2\text{CaCu}_2\text{O}_8$  intrinsic Josephson junction stacks. We show that electrothermal domains dominantly arise from an interplay of Joule heating, caused by the out-of-plane resistance of the stacks, and the in-plane as well as the out-of-plane thermal conductivity of  $\text{Bi}_2\text{Sr}_2\text{CaCu}_2\text{O}_8$ . By contrast, the superconducting transition is not essential for the electrothermal domain formation and as a result the maximum temperature of the hot domains is not necessarily above the superconducting transition temperature  $T_c$ . Still, in most cases this maximum temperature is considerable above  $T_c$ . In simulations, we reproduce numerous effects experimentally observed in previous papers on hot spot formation in intrinsic Josephson junction stacks, making us confident that the description given in this paper captures the essential physics.

PACS numbers: 74.50.+r, 74.72.-h, 85.25.Cp

## I. INTRODUCTION

Joule heating is an omnipresent issue in current-carrying structures and has been studied for a long time. General aspects, like the propagation of switching waves or the formation of static electrothermal domains (ETDs) in bistable conductors are well-known phenomena [1]. In Josephson junctions heating often is small enough to be neglected. An exception are stacks of intrinsic Josephson junctions (IJJs) in the high temperature superconductor  $\text{Bi}_2\text{Sr}_2\text{CaCu}_2\text{O}_8$  (BSCCO). Here, the BSCCO crystal structure intrinsically forms stacks of Josephson junctions, each having a thickness of 1.5 nm. A single IJJ may carry a voltage  $V$  of some mV and a current  $I$  of several mA. Although the dissipative power generated by a single IJJ is only some  $\mu\text{W}$ , the power inside a stack of, say, 1000 IJJs amounts to several mW, with power densities well in excess of  $10^4 \text{ W/cm}^3$ . For small sized ( $\sim$  a few  $\mu\text{m}$  in diameter, consisting of some 10 IJJs) stacks the corresponding overheating has been discussed intensively in literature [2–9].

Recently, coherent off-chip THz radiation with an extrapolated output power of some  $\mu\text{W}$  was observed from stacks of more than 600 IJJs, with lateral dimensions in the  $100 \mu\text{m}$  range [10]. The IJJ stacks have been patterned in the form of mesa structures, as shown schematically in Fig. 1. THz radiation emitted from such IJJ stacks became a hot topic in recent years, both in terms of experiment [10–26] and theory [27–51].

For these mesas there are two regimes where emission occurs [13, 19]. At moderate input power (“low-bias regime”) there is only little heating ( $\lesssim 10 \text{ mW}$ ), and the temperature distribution in the mesa is roughly homogeneous and close to the bath temperature  $T_b$ . The THz emission observed in this regime presumably can be described by more or less standard Josephson physics. At high input power (“high-bias regime”) a hot spot forms inside the mesa [13, 18, 19]. The hot spot effectively separates the mesa into a “cold” region, which is superconducting, and a hot part, which is in the normal state. The “cold” part of the mesa is responsible for THz generation by the Josephson effect. At least for mesas, the hot spot also seems to play a role for synchronization [18, 19, 26]. It has been found that the size and position of the hot spot, and in consequence also the THz emission, can be manipulated by applying proper bias currents across the mesa [18]. Thus, in order to understand the mechanism of THz radiation in IJJ mesas, it seems crucially important to develop a detailed understanding of the hot spot formation. The present paper is devoted to this subject.

In superconducting structures hot spots usually appear, because the sample is (locally) heated to above  $T_c$  [1, 52], i.e. because the sample resistance  $R$  rises from zero to some finite value. By contrast, to obtain THz emission, IJJ stacks are typically biased in a state where all junctions are in their resistive state. Thus, the out-of-plane resistance  $R_c$  is never zero and even has been shown to increase continuously when cooling the sample through  $T_c$  [53, 54]. Superconductivity and a zero resistance state is still present for in-plane currents flowing along the  $\text{CuO}_2$  layers. However, even in their resistive state these layers add only a minor contribution to the total voltage across the IJJ stack and thus to the overall power dissipation due to the huge ratio  $\rho_c/\rho_{ab} > 10^5$  of

\*Electronic address: hbwang1000@gmail.com

†Electronic address: kleiner@uni-tuebingen.de

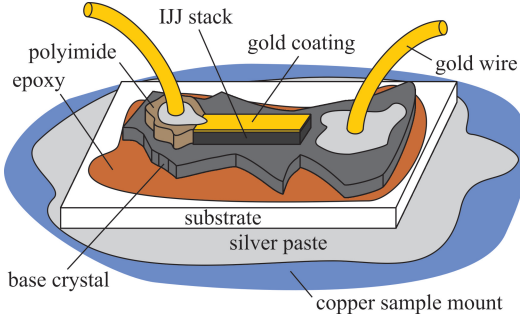


Figure 1: (Color online) Typical design of BSCCO IJJ mesas.

the out-of-plane to the in-plane resistivity. It is unlikely that this contribution gives rise to hot spot formation. Also the BSCCO thermal conductance varies relatively weakly with temperature [55]. Recently, Yurgens et al. have simulated the thermal heating and the temperature distribution in BSCCO IJJ mesas [45, 46], using a 3D finite-element software. The electrical and thermal properties of the various current carrying and insulating layers, cf. Fig. 1, were taken into account. The formation of a hot spot region, as observed in [13], was reproduced qualitatively. Still, the occurring electrothermal phenomena need some discussion, particularly in view of their origin and a quantitative analysis. For example, it is not quite clear yet which of the many electrical and thermal quantities involved are actually responsible for hot spot formation. Also, the current-voltage characteristics (IVCs) presented in [45, 46] do not exhibit the experimentally observed abrupt change in differential resistance when the hot spot appears.

In the underdoped BSCCO we discuss here, in contrast to  $\rho_{ab}$ ,  $\rho_c$  has a negative temperature coefficient below room temperature. In the 1930's Spence and co-workers theoretically investigated IVCs and the thermal breakdown of negative temperature coefficient elements [56–58]. The main effect considered was the formation and stability of ETDs. Although the effects discussed in these papers have nothing to do with superconductivity, the calculated IVCs strongly resemble the IVCs measured for IJJ mesas. The quantity in common is the strong negative temperature coefficient. To our impression, the works by Spence and co-workers contain the key elements of the thermal physics observed in the BSCCO mesas. Thus, below we will refer to the hot areas created in the BSCCO mesas as ETDs, to emphasize the underlying negative temperature coefficient effect. The presence of the Josephson effect, i.e. THz radiation, the formation of electromagnetic standing waves, interactions between ETDs and waves etc. is not considered in this study. This approach to ETD formation seems justified, since the emitted radiation power is 3–4 orders of magnitude lower than the dc input power.

The paper is organized as follows. In Sec. II we consider a simple discrete resistor model to get a basic understanding of the heating phenomena involved. In Sec. III a 1D model is discussed which is extended to 3D and

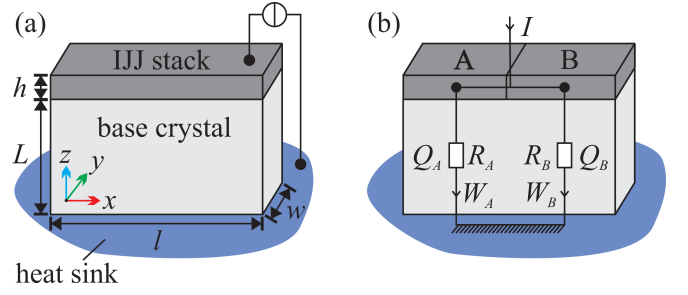


Figure 2: (Color online) Discrete approximation for a mesa. (a) Dimensions of mesa and base crystal. (b) The mesa is replaced by two vertically cooled resistors  $R_A$  and  $R_B$  producing Joule heat  $Q_A$  and  $Q_B$ , which is vertically transported to a thermal bath via heat-transfer powers  $W_A$  and  $W_B$ .

realistic sample geometries in Section IV. The discussions in these sections are based on the thermal and electrical parameters of the BSCCO crystals, as used in experiment. In Sec. IV we address experimental observations, as made in [13, 18, 19, 26]. Sec. V concludes our work.

## II. DISCRETE RESISTORS

The electrothermal behavior of conducting materials can be investigated by considering the heat balance equation between Joule self-heating  $Q(T, \lambda)$  and the heat transfer power  $W(T)$  to the coolant [1]:

$$Q(T, \lambda) = W(T) \quad (1)$$

Here,  $\lambda$  is some control parameter (in our case, voltage  $V$  or current  $I$  across the sample).

We first study the model of two current-biased resistors  $R_A(T_A)$  and  $R_B(T_B)$  connected in parallel, each representing one half of a mesa of length  $l$ , width  $w$  and height  $h$ , cf. Fig. 2.  $T_A$  and  $T_B$  are the temperatures of these resistors.  $R_A$  and  $R_B$  shall be equal for  $T_A = T_B$ . Joule heating is produced via  $Q_i = I_i V_i$ , where  $i = (A, B)$ . The total current is  $I = I_A + I_B$  and further  $V_A = V_B$ , i.e. we neglect the voltage drop due to in-plane currents. The resistors are thermally connected to a bath (temperature  $T_b$ ), which, at a distance  $L$  (the thickness of the base crystal) removes heats  $W_A$  and  $W_B$  “vertically”, through the BSCCO out-of-plane thermal conductivity  $\kappa_c$ .

We first assume  $T_A = T_B = T$ . Then, the IVC of the mesa can be parametrized by  $T$ , using Eq. (1) [59]. With Ohm’s law  $V = R(T) I$ , Newton’s law of cooling

$$W(T - T_b) = \frac{l w}{L} \int_{T_b}^T \kappa_c(\vartheta) d\vartheta \quad (2)$$

and the resistance of the mesa

$$R(T) = \frac{h}{l w} \rho_c(T), \quad (3)$$

we arrive at the following parametrization of the IVC

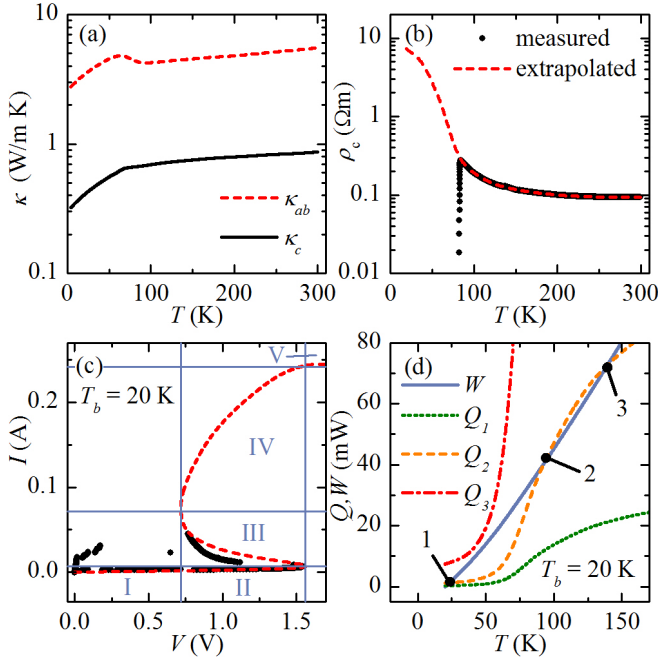


Figure 3: (Color online) (a) Temperature dependence of BSCCO in-plane ( $\kappa_{ab}$ ) and out-of-plane ( $\kappa_c$ ) thermal conductivity [55]. (b)  $c$ -axis resistivity  $\rho_c$ , as measured for a  $330 \times 50 \mu\text{m}^2$  wide and  $0.72 \mu\text{m}$  thick sample for  $T > T_c = 83\text{ K}$ . For lower  $T$ ,  $\rho_c$  has been extrapolated by fitting the IVC, measured at  $T_b = 20\text{ K}$ , using the full 3D heat diffusion equation, cf. Sec. IV. (c) IVC, calculated in the two-resistor model of Sec. II for a homogeneous temperature in the mesa (dashed curve). For comparison, solid circles show the measured IVC. Sectors I–V are explained in the text. (d) Joule self-heating  $Q(T, V)$  and the heat-transfer power  $W(T)$  vs  $T$  (adapted from [1]), using the electrical and thermal parameters of graphs (a) and (b) and assuming a homogeneous temperature distribution.  $Q$  is plotted for 3 voltages  $V = 0.4\text{ V}$  ( $Q_1$ ),  $0.74\text{ V}$  ( $Q_2$ ) and  $1.8\text{ V}$  ( $Q_3$ ). Labels 1, 2 and 3 indicate the graphical solutions to Eq. (1) for  $Q_2$ .

[56–58]:

$$V = \sqrt{R(T)W(T - T_b)}; \quad I = \sqrt{\frac{W(T - T_b)}{R(T)}}. \quad (4)$$

For further calculations, for  $\kappa_c$  the data from [55] are used and extrapolated to lower temperature, cf. Fig. 3 (a). Above the critical temperature  $T_c$  we obtained  $\rho_c(T)$  from the out-of-plane resistance of one of our mesas, cf. solid circles in Fig. 3 (b). Below  $T_c$ ,  $\rho_c(T)$  is extrapolated by fitting the measured IVC of the mesa at a bath temperature of 20 K (see below), using the full 3D heat diffusion equation.  $L = 17 \mu\text{m}$  is chosen, which is a typical value for the thickness of the BSCCO base crystal of the samples we want to discuss [13, 18, 19, 26]. Length, width and height of the mesa are, respectively, taken to be 330, 50 and  $1 \mu\text{m}$ , representing sample 1 from [19]. With these dependencies, the calculated IVC of the mesa is S-shaped and shows a region of negative differential resistance, cf. dashed curve in Fig. 3(c). For comparison the graph also shows by solid circles the measured IVC

at  $T_b = 20\text{ K}$ .

For S-shaped IVCs thermal bistability can occur, since Eq. (1) holds for more than one value of  $T$ . Here for  $V$  between 0.7 and 1.6 V, corresponding to sector II, III and IV in Fig. 3(c) three solutions appear. Since  $\rho_c$  decreases with  $T$ , the control parameter is  $V$  [1]. Figure 3 (d) depicts the graphical solution to Eq. (1). To calculate  $W$  and  $Q$  we used Eq. (2) and  $Q(T, V) = V^2/R(T)$  at  $T_b = 20\text{ K}$ . For small values of  $V$  (sector I in Fig. 3 (c), heating power  $Q_1$  in (d)) the only solution is a homogeneous temperature distribution somewhat above  $T_b$ . The solution in sector II is alike, however determined by point 1 ( $Q_2$ ) in Fig. 3 (d). Here, also two other possible solutions exist. Analogously, for high  $V$  (sector V,  $Q_3$  and sector IV, point 2 for  $Q_2$ ), the sample has a high homogeneous temperature. The IVC has positive differential resistivity for all these solutions. In sector III, the IVC has negative differential resistivity. However, for  $T_A = T_B$  this solution is unstable and the resistors switch from point 2 in Fig. 3 (d) to either point 1 (cold) or point 3 (hot) [1, 60].

Under voltage bias it is hard if not impossible, to reach a steady state where one resistor is cold, while the other is hot: When increasing  $V$  from zero, both resistors are cold until the maximum voltage  $V_0$  ( $\approx 1.6\text{ V}$  in Fig. 3 (c)) is reached. Then, both resistors must switch to a very high current (hot resistors), cf. sector V in Fig. 3 (c). When decreasing  $V$  from this state – assuming that the sample has not yet melted – both resistors remain hot, until near  $V = 0.7\text{ V}$  switch-back to the cold state occurs. Thus, a hysteresis appears in the IVC and a potential hot/cold state has been avoided.

By contrast, a current-controlled system can be forced into this regime. We assume for the following, that  $I$  and thus  $Q$  is increased from zero step-by-step. Fig. 4 (a) and (b) show the individual IVCs of resistor A and B respectively, while (c) shows the IVC of the whole mesa. For small  $Q$  the temperature is the same in both resistors and they carry the same current. In principle, further increase of  $I$  would make the whole mesa pass the point  $\delta$  of local maximal voltage  $V_0$ , cf. Fig. 4 (c) and enter the unstable area of negative differential resistance. This is exemplarily indicated for point  $\alpha$  in Fig. 4 (c). Here, the two resistors with equal temperature  $T_\alpha$ , would be in states  $\alpha_A$  and  $\alpha_B$ , cf. Fig. 4 (a) and (b) respectively. The instability and the constraints of equal voltage and fixed current force the mesa into the state  $\beta$ , which is composed of state  $\beta_A$  with  $T_{\beta_A} > T_\alpha$  and  $\beta_B$  with  $T_{\beta_B} < T_\alpha$ , cf. Fig. 4 (a) and (b) respectively. Another solution satisfying  $V_A = V_B$  would be the combination of point  $\gamma_A$  in Fig. 4 (a) and  $\beta_B$  in (b), which, however, violates current conservation. Thus the combination of  $\beta_A$  and  $\beta_B$  is the only stable solution. The resulting total IVC of Fig. 4 (c) follows the path indicated by the dashed (red) line, differing in voltage from the isothermal case (solid blue line). With increasing  $I$ , starting from point  $\delta$ , the points  $\beta_A$  and  $\beta_B$  “move” towards lower voltage. Note that this implies, that the cold resistor becomes colder while the hot resistor keeps increasing its temperature.

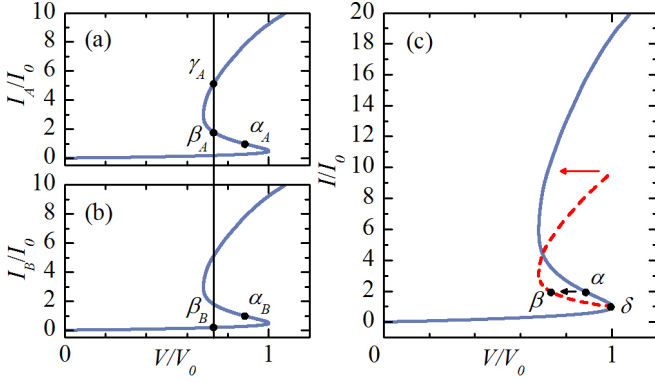


Figure 4: (Color online) ETD formation in a two-resistor model, cf. Fig. 2(b). (a) and (b) display the IVCs of the two individual parts A and B, respectively. (c) shows the IVC of the combined system. The axes are normalized to the current (voltage) of the point showing local maximal voltage  $V_0$ . The total current through the mesa at  $V_0$  is  $I_0$ . The bias points indicated by Greek characters are discussed in the text. In (c) for the solid (blue) curve resistors A and B are at the same temperature, while for the dashed (red) curve their temperature differs, corresponding to ETD formation in the continuous case.

When  $\beta_A$  has reached the minimal voltage, both  $\beta_A$  and  $\beta_B$  start to move towards larger voltage, i.e. also the temperature of the cold part starts to increase. Finally, when  $\beta_B$  reaches the voltage  $V_0$ ,  $T_A \neq T_B$  becomes impossible and the mesa switches back to the homogeneous solution.

The model of two parallel resistors can be extended by several ways: First, an in-plane thermal coupling  $W_{AB}$  between resistors A and B may be included. Then, the cold part will cool the hot part and (thermal) differences between A and B will be less severe. This will shift the point, where the homogeneous solution and the solution  $T_A \neq T_B$  fork, to higher input power [56, 58]. Also, the difference in voltage between the homogeneous and the inhomogeneous solution will be diminished [56, 58]. A detailed discussion, however, is out of the scope of this qualitative section. In-plane cooling will be taken into account in the subsequent sections. Second, one may allow the two resistors (the area of the “hot” and “cold” parts) to be unequal and variable in size. Then, one faces a continuous set of solutions. Third, one may consider more than two resistors in parallel. This would be also applicable to the description of arrays of IJJ stacks, which are interesting for obtaining a large THz emission output power. In this scenario, the whole system will tend to a state, where only one of the stacks is hot, while all the others are cold [58].

### III. 1D MODEL

In this section we consider a 1D continuous model to find the temperature distribution in the mesa for the simplest continuous case, still treating ETD formation from

a generic point of view. I.e., we assume a thin (along  $z$ ) and narrow (along  $y$ ) mesa, neglecting  $T$ -variations along  $z$ - and  $y$ -direction in the mesa (see [1, 58] for details). Then,  $T = T(x)$  is defined by the heat diffusion equation:

$$-\kappa_{ab}(T) h T'' + \frac{\kappa_c(T)}{L} T = \frac{V^2}{\rho_c(T) h} \quad (5)$$

The first term describes the thermal diffusion in  $x$ -direction and the second one the cooling due to the base crystal with the coefficient  $\kappa_c/L$  regulating its strength. The third term represents Joule heating. The sample dimensions  $L$ ,  $h$ ,  $l$  and  $b$  are defined in Fig. 2 (a). We use  $L = 19 \mu\text{m}$ ,  $h = 1 \mu\text{m}$ ,  $l = 330 \mu\text{m}$ ,  $b = 50 \mu\text{m}$  and  $\kappa_{ab}$ ,  $\kappa_c$  and  $\rho_c$  as in Figs. 3 (a), (b). The boundary conditions are chosen to be  $T'(x=0) = T'(x=l) = 0$ , where the prime denotes derivative with respect to  $x$ . These boundary conditions neglect edge cooling. Further, we want to solve Eq. (5) for a given current  $I$  rather than for a given voltage  $V$ . We achieve this by using

$$V = \frac{I h}{\int \sigma_c(T) dx dy}, \quad (6)$$

where  $\sigma_c = 1/\rho_c$  is the  $c$ -axis conductivity. We numerically solve this equation using finite element analysis [61]. Note that Eq. (5) always has a homogeneous solution. To find a nontrivial  $T(x)$ , a proper initial function  $T_i(x)$  has to be used. A calculated IVC for  $T_b = 20$  K is shown in Fig. 5 (a). It resembles the shape of the IVC of the two-resistor model, cf. Fig. 4. Figure 5 (b) shows the temperature in the mesa for the homogeneous solution at the bias points indicated in (a). One notes that up to quite high currents  $\sim 40$  mA the mesa temperature is below  $T_c$ . Figure 5 (c) shows solutions for the bias points indicated in the IVC, when an ETD has formed. Here, the temperature in the hot part rises rapidly to temperatures well above  $T_c$ , while the temperature of the cold part is near  $T_b = 20$  K. Also, one observes, that the hot part grows in size when  $I$  is increased. Further note, that in the presence of an ETD the temperature  $T_{cold}$  of the cold part is below the temperature of the homogeneous solution for the same value of  $Q$ ;  $T_{cold}$  decreases with increasing  $Q$ , and finally converges against a limiting value. The strength of the deviation of the ETD temperature profile from the homogeneous solution directly correlates with the strength of branching in the IVC. In the depicted case the branching is very strong, which is due to a small ratio of the in-plane to the out-of-plane thermal coupling, cf. first and second term in Eq. (5).

For a given  $I$  the ETDs presented in Fig. 5 (c) are not the only possible solutions to Eq. (5) [62]. For symmetry reasons also the mirrored solution exists, as well as solutions with the hot domain near and in the center of the mesa, cf. Fig. 5 (d). In the IVC the different solutions slightly differ in  $V$  and can be traced over some range in  $I$ . Thus, the ETD part of the IVC consists of several branches distinguishing specific kinds of domains. Experimentally, in some cases, hot spot formation



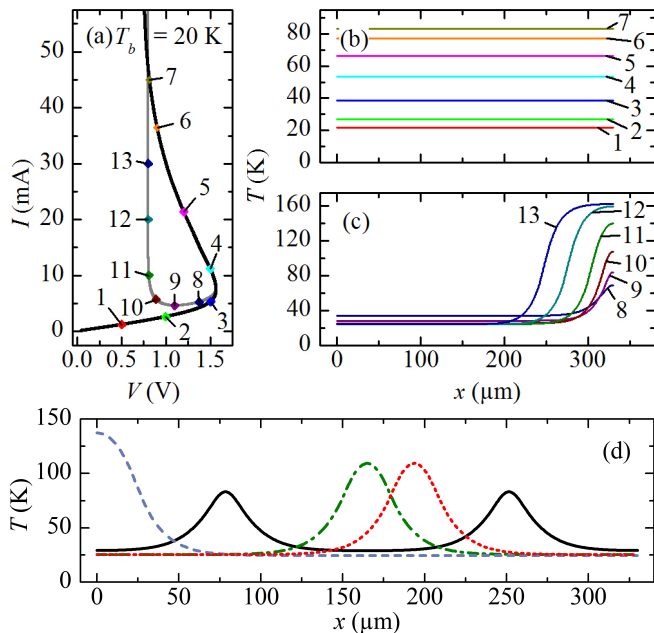


Figure 5: (Color online) Simulation results of Eq. (5) for  $T_b = 20$  K and  $L = 19 \mu\text{m}$ . Other mesa dimensions are listed in Sec. II. Graph (a) shows the IVC for the homogeneous solution (black curve) and a ETD solution showing a hot domain on the right mesa end (gray curve).  $T(x)$ -profiles are displayed in (b) for the homogeneous case and in (c) for the ETD case. The numbers indicate the bias points on the IVC. In (d)  $T(x)$ -profiles, obtained from different  $T_i(x)$ , are shown for solutions with  $I = 9.5$  mA, exhibiting various shape and positioning of the hot domain.

in different places of the mesa has been detected by low-temperature scanning-laser microscopy (LTSLM). However, usually a specific configuration is much more stable than the others, presumably due to inhomogeneities like attached wires. In the calculations, also solutions with more than one hot domain [63] can be found, cf. Fig. 5 (d). However, this has not been observed in any of our LTSLM measurements. It is argued in [58], that such a state is very unstable and will not occur, since the sample can be seen as a parallel circuit of several discrete parts with small thermal coupling between them, cf. section II.

#### IV. 3D MODEL

In this section we address ETD formation in 3D. The goal is to quantitatively compare our experimental observations with the numerical simulations [61]. We thus, similarly as in [45, 46], also include various electrically and thermally conducting and insulating layers that are in contact with our BSCCO mesas. The geometry used is still somewhat simplified compared to the real samples but should allow to capture the relevant physics. Figure 6 depicts the model. The substrate is omitted and a boundary condition  $T_b = \text{const.}$  is applied to the bottom surface of the glue layer, representing the bath temper-

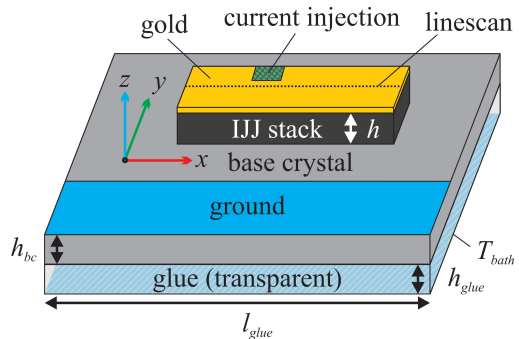


Figure 6: (Color online) Model geometry of the mesa.

ature. This simplification can be done with almost no impact on the results for the mesa, since the thermal conductivity of the substrate (e.g sapphire) is by far better than that of the glue layer. The geometric dimensions of the mesa, the thicknesses of the glue layers ( $10 - 30 \mu\text{m}$ ) and of the gold coatings ( $h_{Au} \approx 30$  nm) were roughly chosen as in the real samples. The base crystal's lateral size is typically of the order of 1 mm, while its thickness  $h_{bc}$  may vary from roughly ten to several hundred  $\mu\text{m}$ , strongly depending on the fabrication process. The current leads are simply represented by boundary conditions on the surfaces of either the gold layer on the mesa or on the base crystal. The current is injected through a  $20 \times 10 \mu\text{m}^2$  rectangle and the current sink is defined as a ground of large area (roughly  $0.3 \text{ mm}^2$ ), cf. Fig. 6.

The equation to be solved is [46]:

$$-\nabla [\kappa(T(\mathbf{r})) \nabla T(\mathbf{r})] = \rho(T(\mathbf{r})) \mathbf{j}^2(\mathbf{r}), \quad (7)$$

where  $\rho$  and  $\kappa$  are the resistivity and thermal conductivity tensor, respectively, and  $\mathbf{r}$  is the spatial coordinate. Unlike the mesa, the base crystal is not always in the resistive state. We model its resistance by using the  $\rho_c$  vs.  $T$  data indicated by solid circles in Fig. 3 (b). The in-plane resistivity  $\rho_{ab}$  is the same for both mesa and base crystal; we use the same  $T$  dependence as in [46]. The thermal conductivity for BSCCO is used from [55], cf. Fig. 3 (a). Thermal and electrical conductivity for a 30 nm thick Au film are adopted from [64]. For the thermal conductivity  $\kappa_{\text{glue}}$  of the glue between the BSCCO base crystal and the substrate to first order we use the polyimide data of [65]. Since our glue might have slightly different properties we in addition multiply  $\kappa_{\text{glue}}$  with a factor  $n_{\text{glue}}$ , which we fit by adjusting the calculated IVC to the measured one.

The base crystal introduces an effective side-cooling of the mesa, which in general makes a solution showing variation in  $x$  and  $y$  direction (with or without ETDs) favorable. Indeed, in contrast to the one-dimensional calculations, ETD solutions appeared basically by themselves, i.e. it was not necessary to find them by choosing a proper initial condition. The side-cooling leads to an elliptic shape of the hot domain (for rectangular shaped mesas). Also, the hot domain is not limited to the mesa itself anymore, but may extend significantly in lateral di-

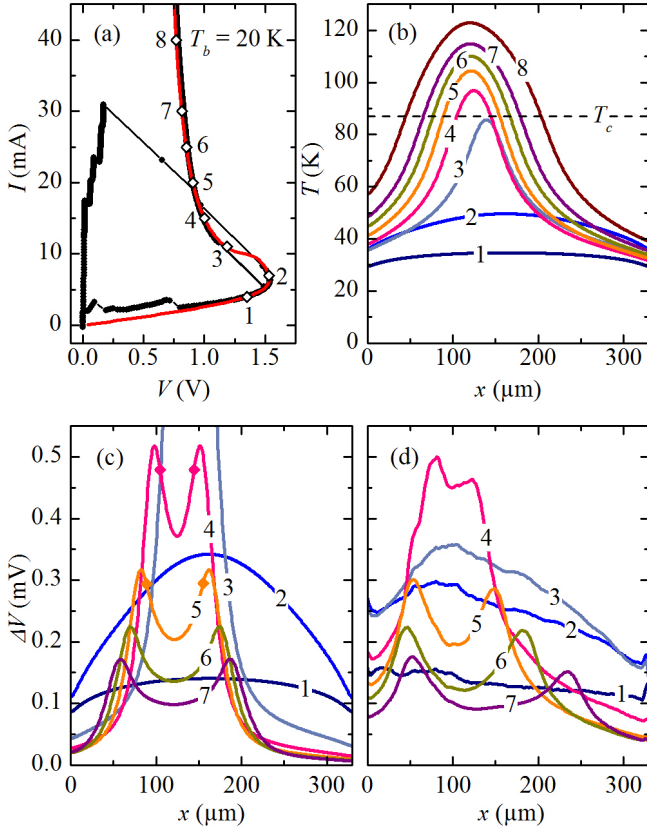


Figure 7: (Color online) Comparison of 3D simulation and experimental data for sample 1 from [19] at  $T_b = 20$  K. (a) shows the measured (black, solid circles) and simulated (red solid line) IVCs. In (b) simulated  $T(x)$ -profiles along the dashed line indicated in Fig. 6 at  $z = 0.5h$  are shown. The diamonds in (a) indicate the corresponding bias points. The calculated and measured  $\Delta V(x)$  are shown in (c) and (d), respectively. Diamonds in (c) indicate the  $x$ -position where  $T = T_c$ .

rection into the base crystal (see below). This is exactly what has been found experimentally [18]. The same occurs in  $z$ -direction, as has been discussed in [46].

We investigate sample 1 from [19]. The electrical and thermal parameters of this sample have already been used in the previous sections. We have further used the parameters:  $h_{bc} = 40 \mu\text{m}$ ,  $h_{glue} = 25 \mu\text{m}$ ,  $l_{glue} = 1 \text{ mm}$  and  $n_{glue} = 1.95$ . Figure 7 (a) compares the measured IVC with the calculated one for  $T_b = 20$  K. The good agreement stems from the fact that we have adjusted  $\sigma_c(T)$  below  $T_c$  and  $n_{glue}$  to match this curve. The simulated  $T(x)$ -profiles, calculated along the dashed line in Fig. 6 at  $z = 0.5h$ , are shown in Fig. 7 (b) for the bias points indicated in Fig. 7 (a). They show an almost constant temperature in the low bias regime, whereas for increasing current the hot domain forms by the growth of a buckling in the  $T(x)$ -profile (compare curves 2 and 3 in Fig. 7 (b)). Further increasing  $I$  and thus  $Q$  leads to a growth in diameter and maximal temperature of the hot domain (curves 4 to 8). Note that  $T_c$ , indicated by the horizontal dashed line, can be significantly exceeded in the center of the hot domains, confirming the results in

[46].

We next want to provide a quantitative comparison between the ETD signals observed in LTSLM [13, 18, 19] and the calculated temperature distributions for this sample. The analysis of the LTSLM signal follows the analysis given in [66]. In LTSLM the laser spot causes a change  $\Delta V(x_0, y_0)$  in the voltage  $V$  across a sample, approximately given by

$$\Delta V(x_0, y_0) = \frac{-IR_{eff}^2 \Delta T A_L}{h} \frac{d\sigma_c}{dT}(T(x_0, y_0)). \quad (8)$$

Here we assumed that the laser is positioned at  $(x_0, y_0)$  and causes, within a Gaussian profile (which, in this paper, we assume to be narrow compared to the temperature variations in the mesa), a maximum temperature rise  $\Delta T \sim 1\text{--}3$  K, depending on the laser power.  $R_{eff} = V/I$  is the (ohmic) sample resistance at a given  $I$  and  $A_L$  is the effective area warmed up by the laser (some  $\mu\text{m}^2$ ).  $\frac{d\sigma_c}{dT}(T(x_0, y_0))$  denotes the temperature derivative of the  $c$ -axis electrical conductivity. The calculated and measured  $\Delta V$ , taken at various bias points indicated in Fig. 7 (a), are shown in Fig. 7 (c) and (d), respectively. For the simulations we have used  $\Delta T \cdot A_L = 56 \text{ K}\mu\text{m}^2$ . The product makes sense, since we expect a temperature rise  $\Delta T \sim 2$  K and  $A_L \sim 5 \mu\text{m}^2$  for the samples we discuss here. The agreement with the experimental curves is reasonable, although differences occur at low bias and near the ETD nucleation point. Particularly, for the bias points 1 and 2, the simulation yields a parabolic shape of  $\Delta V$ , while the experimental data are shaped less regular. Note, however, that in these regions the supercurrents, which are basically neglected in our analysis, may play a major role. For curve 3 in the simulation ETD formation has already occurred, while in experiment the mesa is close to, but still slightly before the nucleation point. For a bias well above this point theoretical curves and experimental data agree well. Specifically the double hump feature in  $\Delta V(x)$  is reproduced correctly in the simulations. The local temperature at the maxima in  $\Delta V$  corresponds to the temperature  $T^* \approx 80$  K, for which  $d\sigma_c/dT$  is maximum, cf. Eq. (8). Between the two  $\Delta V$  maxima,  $T > T^*$ . By coincidence,  $T^* \approx T_c$ ; the diamonds in Fig. 7 (c) indicate the locations for which  $T = T_c$ . Thus, the border between superconducting and non-superconducting parts, which is important for THz emission, can be approximately identified by the position of the humps.

We next investigate the dependence of ETD formation on  $T_b$ . Figure 8 shows a similar set of data as Fig. 7, but for  $T_b = 42$  K. Here,  $n_{glue} = 3.5$  has been chosen. The transition region between the hot and cold domain is less steep than for  $T_b = 20$  K. Also, the nucleation point of the hot domain has moved to higher currents (10 mA for  $T_b = 20$  K and 14 mA for  $T_b = 42$  K) and the back-bending of the IVC has decreased. These effects arise from the fact that the  $xy$ -plane thermal coupling has increased relative to the out-of-plane thermal coupling [58], cf. Sec. III. Note, that this also means for equal input power, that the hot domain reaches higher and the cold domain

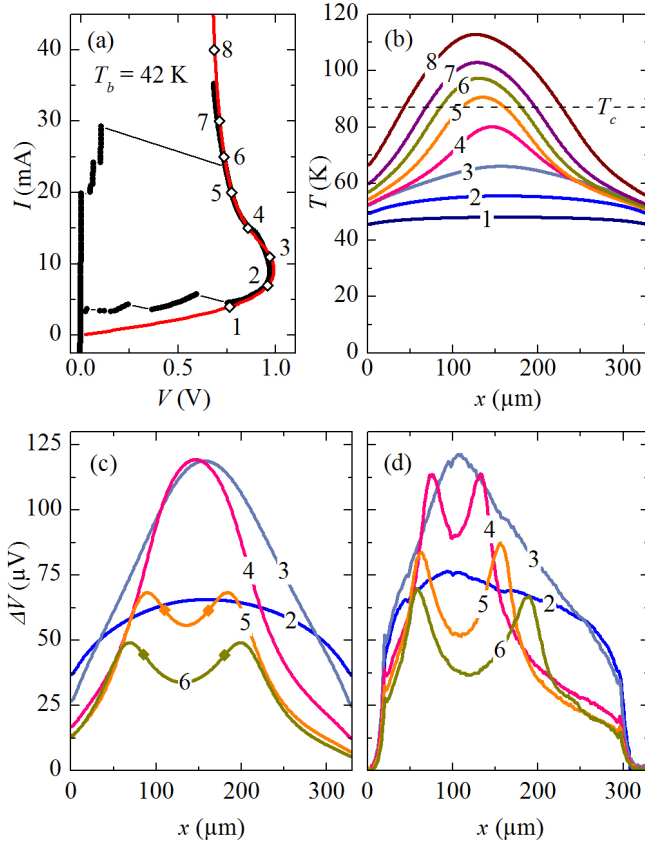


Figure 8: (Color online) Comparison of 3D simulation and experimental data for sample 1 from [19] at  $T_b = 42$  K. (a) shows the measured (black, solid circles) and simulated (red solid curve) IVC. In (b) simulated  $T(x)$ -profiles along the dashed line indicated in Fig. 6 at  $z = 0.5h$  are shown. The diamonds in (a) indicate the corresponding bias points. The calculated and measured  $\Delta V(x)$  are shown in (c) and (d), respectively. Diamonds in (c) indicate the  $x$ -position where  $T = T_c$ .

reaches lower temperatures for  $T_b = 20$  K as for  $T_b = 42$  K. Figures 8 (c) and (d) respectively show the calculated and measured LTSML profiles. As for 7 (c) and (d) the agreement between experimental data and simulations is reasonable, except for the bias point where ETD formation sets in (curve 4). For the calculations we have used  $\Delta T \cdot A_L = 16 \text{ K}\mu\text{m}^2$ , which is by a factor of 3 lower than for the case of  $T_b = 20$  K. This is attributed to a reduced incident laser power, which had been readjusted for every measurement.

In Fig. 9 (a), we show the  $T(x)$ -profile, calculated along the dashed line in Fig. 6 at  $z = 0.5h$ , for 3 values of  $T_b$ . For all curves,  $V = 0.8$  V. This condition has been motivated by measurements of the linewidth  $\Delta f$  of THz radiation [26]. Here, for  $\Delta f$  vs.  $T_b$ , taken at a fixed emission frequency (corresponding to  $V = \text{const.}$  for a fixed number of oscillating IJJs) the dependence  $\Delta f \propto T_b^{-4}$  has been found unexpectedly. We are interested in the question whether or not corresponding changes with  $T_b$  can be seen in the  $T$  distribution in the mesa. Figure 9 (a) shows, that the peak temperature in the mesa is higher at low  $T_b$  than at high  $T_b$ , while the coldest temperatures,

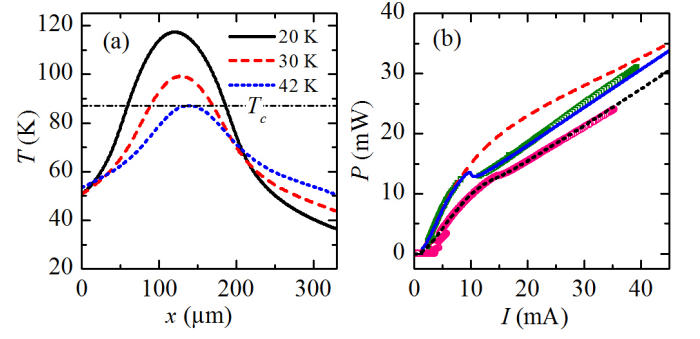


Figure 9: (Color online) (a) Simulated  $T(x)$ -profiles along the dashed line indicated in Fig. 6 at  $z = 0.5h$  for three different values of  $T_b$  at constant  $V = 0.8$  V. The dc power  $P = IV$  is 26.4, 18.2 and 14.4 mW for  $T_b = 20, 30$  and 42 K, respectively. (b)  $P$  vs.  $I$  at 20 K for measurement (green squares), simulation with homogeneous  $T$  (red dashed line) and ETD formation (blue, solid line). The pink circles depict experimental data and the black, short-dashed line simulated values with ETDs at 42 K.

reached at the right edge of the mesa, behave oppositely. Thus, thermal gradients at low  $T_b$  are stronger than at high  $T_b$ . However, this effect roughly changes linearly with  $T_b$  and presumably cannot explain the  $\Delta f \propto T_b^{-4}$  dependence.

Figure 9 (b) compares for two values of  $T_b$  the measured and simulated DC power  $P = IV$  as a function of  $I$ . One observes two regimes, each with a roughly constant slope. The first – low-bias – regime has no hot domain and, for  $T_b = 20$  K, spans from 0 to 10 mA (14 mA for 42 K), whereas the second – high-bias – regime has a hot domain and begins at 10 mA (14 mA for 42 K). Interestingly, at the intersection of these two regimes the maximum temperature in the mesa has reached the temperature fulfilling  $d\sigma_c/dT = 0$ . This point also corresponds to the kink in the IVC, observed for several mesas. Note that the calculation for homogeneous  $T$  (red dashed curve) shows no such kink. A plot like this may thus be helpful to distinguish in an experiment, whether or not one has reached the regime with ETDs.

The last issue we want to address is the correlation between the point of current injection and the location, where the hot domain is established. Typically, in experiment the appearance of the hot domain was close to, but not exactly at the bond wire to the mesa surface [18]. We see the same effect in our simulations, Fig. 10 (a) illustrates this for a situation, where the current is injected from the left. Here, the side-cooling prevents the hot domain from nucleating at the very left end of the mesa, resulting in a positioning of the hot domain at several  $\mu\text{m}$  right of the current injection point. Further, it has been shown that by using two injectors located on opposite sides of the mesas the hot domain can be moved by changing the ratio of currents through these injectors [18]. Figure 10 (a)–(d) show a sequence of calculations where the ratio between injection currents through the left (current  $I_l$ ) and right (current  $I_r$ ) was varied, keeping the sum of the currents  $I_0$  constant. We used ratios

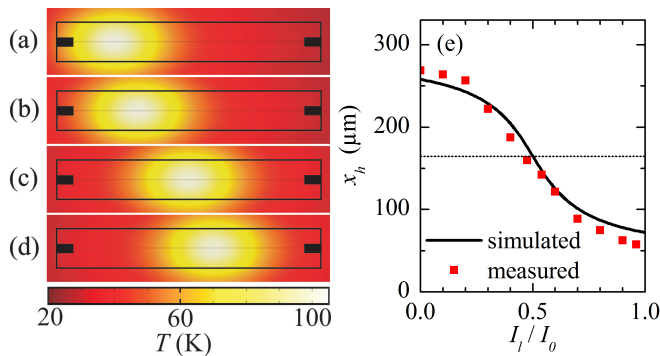


Figure 10: (Color online) (a)–(d) Surface plot of ETD solutions, obtained by Eq. (7) for a mesa with two current injection points, indicated by black rectangles. The sum  $I_0$  of the currents through the left ( $I_L$ ) and right ( $I_R$ ) injection points has been kept constant, and for the ratio  $I_L/I_0$  values of (a) 1, (b) 0.7, (c) 0.5 and (d) 0.425 have been used. Graph (e) shows the center position  $x_h$  of the hot domain vs. current injection ratio for simulated and measured data.

$I_L/I_0$  of, respectively, 1, 0.7, 0.5 and 0.425. As one can see, the hot domain indeed can be moved continuously, as in experiment. In Fig. 10 (e) we have plotted the center position of the hot domain as a function of  $I_L/I_0$ . Experimental data are shown by (red) squares and theoretical data by the (black) solid line. The agreement is reasonable, showing that this effect can be essentially understood from the thermal calculations presented in this paper.

Finally, we briefly mention that also two other geometries discussed in [18] can be reproduced very well in the 3D simulation – a disk shaped mesa and a mesa of Y shape, where the hot ETD forms at the intersection of the three lines, although the bias current injection point was at the foot of the Y.

## V. CONCLUSION

In conclusion, we have investigated experimentally and numerically the temperature profiles and “hot spot” for-

mation in IJJ mesas. We have shown, that the hot spots dominantly arise from the negative temperature coefficient of the out-of-plane resistance of the mesas. Consequently, the *superconducting* properties are not essential. Very similar effects have been observed and analyzed in *semiconducting* structures, and the expression used in this context – the formation of electrothermal domains – seems more proper to describe the situation observed in intrinsic Josephson junction stacks. The interplay between Joule heating, in-plane and out-of-plane thermal conductivity of BSCCO, as well as thermal coupling to the heat sink, governs the strength of electrothermal domain formation. Since the superconducting transition is not essential for the electrothermal domain formation the maximum temperature of the hot domains is not necessarily above  $T_c$ ; however, in most cases this is indeed so. We have given – in the frame of what available data allow – a quantitative comparison between simulation and experiment, showing reasonable agreement. Numerous effects observed in previous papers on domain formation in intrinsic Josephson junction stacks [13, 18, 19] are reproduced by the simulations, making us confident that the description given in this paper captures the essential physics, except for the interplay of ETDs and THz waves. Resolving this issue is a task for the future.

## Acknowledgments

We gratefully acknowledge financial support by the JST/DFG strategic Japanese-German International Cooperative Program and the German Israeli Foundation (Grant No. G-967-126.14/2007). S.G. acknowledges support by AFOSR.

- 
- [1] A. V. Gurevich and R. G. Mints, Rev. Mod. Phys. **59**, 941 (1987).
  - [2] P. Thomas, J. Fenton, G. Yang, and C. Gough, Physica C **341**, 1547 (2000).
  - [3] J. C. Fenton and C. E. Gough, J. Appl. Phys. **94**, 4665 (2003).
  - [4] K. Anagawa, Y. Yamada, T. Shibauchi, M. Suzuki, and T. Watanabe, Appl. Phys. Lett. **83**, 2381 (2003).
  - [5] V. N. Zavaritsky, Phys. Rev. Lett. **92**, 259701 (2004).
  - [6] A. Yurgens, D. Winkler, T. Claeson, S. Ono, and Y. Ando, Phys. Rev. Lett. **92**, 259702 (2004).
  - [7] V. M. Krasnov, M. Sandberg, and I. Zogaj, Phys. Rev. Lett. **94**, 077003 (2005).
  - [8] H. B. Wang, T. Hatano, T. Yamashita, P. H. Wu, and P. Müller, Appl. Phys. Lett. **86**, 023504 (2005).
  - [9] B. Verreet, N. Sergeant, D. M. Negrete, M. Torstensson, D. Winkler, and A. Yurgens, Supercond. Sci. Technol. **20**, S48 (2007).
  - [10] L. Ozyuzer, A. E. Koshelev, C. Kurter, N. Gopalsami, Q. Li, M. Tachiki, K. Kadowaki, T. Yamamoto, H. Minami, H. Yamaguchi, et al., Science **318**, 1291 (2007).
  - [11] K. Kadowaki, H. Yamaguchi, K. Kawamata, T. Yamamoto, H. Minami, I. Kakeya, U. Welp, L. Ozyuzer, A. Koshelev, C. Kurter, et al., Physica C **468**, 634 (2008).
  - [12] L. Ozyuzer, Y. Simsek, H. Koseoglu, F. Turkoglu, C. Kurter, U. Welp, A. E. Koshelev, K. E. Gray, W. K. Kwok, T. Yamamoto, et al., Supercond. Sci. Technol. **22**, 114009 (2009).



- [13] H. B. Wang, S. Guénon, J. Yuan, A. Iishi, S. Arisawa, T. Hatano, T. Yamashita, D. Koelle, and R. Kleiner, *Phys. Rev. Lett.* **102**, 017006 (2009).
- [14] H. Minami, I. Kakeya, H. Yamaguchi, T. Yamamoto, and K. Kadowaki, *Applied Physics Letters* **95**, 232511 (pages 3) (2009).
- [15] K. Kadowaki, M. Tsujimoto, K. Yamaki, T. Yamamoto, T. Kashiwagi, H. Minami, M. Tachiki, and R. A. Klemm, *J. Phys. Soc. Jpn* **79**, 023703 (2010).
- [16] C. Kurter, K. E. Gray, J. F. Zasadzinski, L. Ozyuzer, A. E. Koshelev, Q. Li, T. Yamamoto, K. Kadowaki, W.-K. Kwok, M. Tachiki, et al., *IEEE Trans. Appl. Supercond.* **19**, 428 (2009).
- [17] K. E. Gray, L. Ozyuzer, A. K. C. K. Kurter, K. Kadowaki, T. Yamamoto, H. Minami, H. Yamaguchi, M. T. M, W. Kwok, and U. Welp, *IEEE Trans Appl. Supercond.* **19**, 3755 (2009).
- [18] S. Guénon, M. Grünzweig, B. Gross, J. Yuan, Z. Jiang, Y. Zhong, A. Iishi, P. Wu, T. Hatano, D. Koelle, et al., *Phys. Rev. B* **82**, 214506 (2010).
- [19] H. B. Wang, S. Guénon, B. Gross, J. Yuan, Z. G. Jiang, Y. Y. Zhong, M. Gruenzweig, A. Iishi, P. H. Wu, T. Hatano, et al., *Phys. Rev. Lett.* **105**, 057002 (2010).
- [20] M. Tsujimoto, K. Yamaki, K. Deguchi, T. Yamamoto, T. Kashiwagi, H. Minami, M. Tachiki, K. Kadowaki, and R. A. Klemm, *Phys. Rev. Lett.* **105**, 037005 (2010).
- [21] M. Tsujimoto, T. Yamamoto, K. Delfanazari, R. Nakayama, T. Kitamura, M. Sawamura, T. Kashiwagi, H. Minami, M. Tachiki, K. Kadowaki, et al., *Phys. Rev. Lett.* **108**, 107006 (2012).
- [22] H. Koseoglu, F. Turkoglu, Y. Simsek, and L. Ozyuzer, *J. Supercond. Nov. Magn.* **24**, 1083 (2011).
- [23] T. M. Benseman, A. E. Koshelev, K. E. Gray, W.-K. Kwok, U. Welp, K. Kadowaki, M. Tachiki, and T. Yamamoto, *Phys. Rev. B* **84**, 064523 (2011).
- [24] K. Yamaki, M. Tsujimoto, T. Yamamoto, A. Furukawa, T. Kashiwagi, H. Minami, and K. Kadowaki, *Opt. Express* **19**, 3193 (2011).
- [25] T. Kashiwagi, M. Tsujimoto, T. Yamamoto, H. Minami, K. Yamaki, K. Delfanzari, K. Deguchi, N. Orita, T. Koike, R. Nakayama, et al., *J. J. Appl. Phys.* **51**, 010113 (2012).
- [26] M. Y. Li, J. Yuan, N. Kinev, J. Li, B. Gross, S. Guénon, A. Ishii, K. Hirata, T. Hatano, D. Koelle, et al., *unpublished* (2012).
- [27] L. N. Bulaevskii and A. E. Koshelev, *Phys. Rev. Lett.* **99**, 057002 (2007).
- [28] A. E. Koshelev and L. N. Bulaevskii, *Phys. Rev. B* **77**, 014530 (2008).
- [29] A. E. Koshelev, *Phys. Rev. B* **78**, 174509 (2008).
- [30] S. Lin and X. Hu, *Phys. Rev. Lett.* **100**, 247006 (2008).
- [31] V. M. Krasnov, *Phys. Rev. Lett.* **103**, 227002 (2009).
- [32] X. Hu and S. Z. Lin, *Phys. Rev. B* **80**, 064516 (2009).
- [33] R. A. Klemm and K. Kadowaki, *Journal of Physics: Condensed Matter* **22**, 375701 (2010).
- [34] Y. Nonomura, *Phys. Rev. B* **80**, 140506 (2009).
- [35] M. Tachiki, S. Fukuya, and T. Koyama, *Phys. Rev. Lett.* **102**, 127002 (2009).
- [36] T. Koyama, H. Matsumoto, M. Machida, and K. Kadowaki, *Phys. Rev. B* **79**, 104522 (2009).
- [37] N. Pedersen and S. Madsen, *IEEE Trans Appl. Supercond.* **19**, 726 (2009).
- [38] S. Savel'ev, V. A. Yampol'skii, A. L. Rakhmanov, and F. Nori, *Rep. Prog. Phys.* **73**, 026501 (2010).
- [39] X. Hu and S. Z. Lin, *Supercond. Sci. Technol.* **23**, 053001 (2010).
- [40] T. Tachiki and T. Uchida, *J. Appl. Phys.* **107**, 103920 (2010).
- [41] S. Z. Lin and X. A. Hu, *Phys. Rev. B* **82**, 020504 (2010).
- [42] W. Zhou, C. Wang, and Q.-H. Chen, *Phys. Rev. B* **82**, 184514 (2010).
- [43] A. E. Koshelev, *Phys. Rev. B* **82**, 174512 (2010).
- [44] M. Tachiki, K. Ivanovic, K. Kadowaki, and T. Koyama, *Phys. Rev. B* **83**, 014508 (2011).
- [45] A. Yurgens, M. Torstensson, and D. Winkler, *Physica C: Superconductivity* **470**, 818 (2010).
- [46] A. A. Yurgens, *Phys. Rev. B* **83**, 184501 (2011).
- [47] A. A. Yurgens and L. N. Bulaevskii, *Supercond. Sci. Technol.* **24**, 015003 (2011).
- [48] T. Koyama, H. Matsumoto, M. Machida, and Y. Ota, *Supercond. Sci. Technol.* **24**, 085007 (2011).
- [49] S. Z. Lin and X. A. Hu, *J. Nanoscience and Nanotechnol.* **11**, 2916 (2011).
- [50] S.-Z. Lin, X. Hu, and L. Bulaevskii, *Phys. Rev. B* **84**, 104501 (2011).
- [51] T. M. Slipchenko, D. V. Kadygrob, D. Bogdanis, V. A. Yampol'skii, and A. A. Krokhnin, *Phys. Rev. B* **84**, 224512 (2011).
- [52] W. J. Skocpol, M. R. Beasley, and M. Tinkham, *J. Appl. Phys.* **45**, 4054 (1974).
- [53] A. Yurgens, D. Winkler, N. V. Zavaritsky, and T. Claesson, *Phys. Rev. Lett.* **79**, 5122 (1997).
- [54] Y. I. Latyshev, T. Yamashita, L. N. Bulaevskii, M. J. Graf, A. V. Balatsky, and M. P. Maley, *Phys. Rev. Lett.* **82**, 5345 (1999).
- [55] M. F. Crommie and A. Zettl, *Phys. Rev. B* **43**, 408 (1991).
- [56] E. Spenke, *Electrical Engineering (Archiv fuer Elektrotechnik)* **30**, 728 (1935).
- [57] H. Lueder and E. Spenke, *Physikalische Zeitschrift* **36**, 767 (1936).
- [58] E. Spenke, *Wissenschaftliche Veroeffentlichungen aus den Siemens-Werken* **15**, 92 (1936).
- [59] H. Busch, *Annalen der Physik* **64**, 401 (1921).
- [60] A. F. Volkov and S. M. Kogan, *Soviet Physics Uspekhi* **11**, 881 (1969).
- [61] See [<http://www.comsol.com>] for details.
- [62] Generally, to find a given solution and to trace it out over some current range, the current was first ramped from zero to high currents with a homogeneous temperature distribution. In order to get solutions with domain formation, a proper initial condition for the temperature profile of the ETD solution was made and, if successful, the current was increased or decreased in small steps, resulting in a branch with domain formation.
- [63] In other systems, stable configurations with few or even many hot spots in a sequence were considered for the case, when the out-of-plane resistivity is much higher than the in-plane resistivity [1, 67, 68]. In this case the high out-of-plane resistivity results in an effective self-consistent shunt that is stabilizing the hot spot structure.
- [64] K. L. Chopra, L. C. Bobb, and M. H. Francombe, *Journal of Applied Physics* **34**, 1699 (1963).
- [65] See [<http://cryogenics.nist.gov>] for details.
- [66] R. Werner, M. Weiler, A. Y. Petrov, B. A. Davidson, R. Gross, R. Kleiner, S. T. B. Goennenwein, and D. Koelle, *Appl. Phys. Lett.* **99**, 182513 (2011).
- [67] A. A. Akhmetov and R. G. Mints, *Journal of Physics D: Applied Physics* **16**, 2505 (1983).
- [68] A. A. Akhmetov and R. G. Mints, *Journal of Physics D:*

Applied Physics **18**, 925 (1985).